RSC Advances

ROYAL SOCIETY OF CHEMISTRY

www.rsc.org/advances

Etching synthesis of iron oxide nanoparticles for adsorption of arsenic from water

Wei Cheng, Weidong Zhang, Lijuan Hu, Wei Ding, Feng Wu and Jinjun Li*

School of Resources and Environmental Sciences, Hubei Key Lab of Bioresources and Environmental Biotechnologies, Wuhan University, Wuhan 430079, China

**Corresponding Author*

Tel.: +86 27 68778511. E-mail: ljjcbacademy@163.com

Present address: Wuhan University, No. 129, Luoyu Road, Wuhan, 430079, P. R. China

† Electronic Supplementary Information (ESI) available: Energy-dispersive spectrometry pattern of Fe-Si composite and nano-iron oxide, X-ray diffraction spectrum of nano-iron oxide, Nitrogen adsorption–desorption isotherm of nano-iron oxide, Point of zero charge (PZC) of nano-iron oxide, As(III) and As(V) speciation for various pH values, Influence of initial H_2O_2 concentration on As(III) removal. See DOI:10.1039/x0xx00000x

Abstract

Arsenic contamination in source drinking water has become an alarming issue worldwide. Iron oxides have been recognized as effective adsorbents for arsenic removal. In this study, an etching method was used to synthesize nanosized iron oxide with small primary particle sizes of approximately 4 nm and a high specific surface area of 317 m^2/g. The material was used as an adsorbent for arsenic removal from water. The sorption isotherms fit the Langmuir equation, and the derived maximum sorption capability for As(III) and As(V) is 42 mg/g at pH 7 and 83 mg/g at pH 3, respectively. Arsenic adsorption obeys pseudo-second-order kinetics. The adsorption sites were located mostly on the external nanoparticle surface, and therefore intraparticle diffusion resistance was avoided and external diffusion was the rate-limiting step. The mechanism of arsenic removal on nanosized iron oxide is chemisorption via inner-sphere surface complexation, and the hydroxyl groups of arsenic species are important for reaction with adsorbent surface hydroxyl groups. Adsorption of As(III) in the presence of hydrogen peroxide and ferrous ion was also studied, and the catalytic oxidation of As(III) promoted its adsorptive removal significantly.

1. Introduction

Arsenic contamination has become an alarming issue worldwide because of its high toxicity and carcinogenicity.[1-3] Chronic exposure to arsenic may cause tumors in the liver, lung, kidney, bladder, skin, and various human tissues; lead to cardio vascular system problems; and impede the mental development of children.[4-6] The World Health Organization has lowered the limit of arsenic concentration in drinking water from 50 to 10 μg/L.[2,7] Toxicity, mobility, and bioavailability of arsenic is related to its chemical speciation, oxidation state, and solution pH.[7-9] In natural water, arsenic exists mainly as inorganic arsenate As(V) and arsenite As(III).[1] As(V) predominates in oxidizing conditions and is present mainly as H_3AsO_4 (pH < 2.2), $H_2AsO_4^-$ (2.2 < pH < 7), $HAsO_4^{2-}$ (7 < pH < 11.5), and AsO_4^{3-} (pH > 11.5).[1,4] As(III) is the major arsenic species under reducing conditions and is present mainly as neutral H_3AsO_3 (pH < 9.2), $H_2AsO_3^-$ (9.2 < pH < 12), and $H_2AsO_3^{2-}$ (pH > 12).[1,3]

Adsorption is one of the most promising techniques for arsenic removal from water,[10] and iron oxide is used extensively as an adsorbent because of its high affinity toward arsenic and low cost.[2,11-13] Nanosized iron oxides are desirable for adsorption applications because of their large surface areas.[14] Various methods such as solvothermal reduction[11,15] and thermal decomposition[14,16-18] have been applied in recent years to produce iron oxide nanoparticles. Solvothermal reduction usually involves thermal treatment of ferric salts and organic reducing agents in organic solvents.[11,15] Thermal decomposition involves the decomposition of iron precursors, such as long-chain iron carboxylates,[16] iron acetylacetonate[17] or iron pentacarbonyl $Fe(CO)_5$[14,18] in a high-boiling-point organic solvent. These processes are complicated and high-cost, and usually involve toxic organics.[19] Because of these disadvantages, intensive research is underway to introduce new procedures for the synthesis of iron oxide adsorbents.

As(III) is considered to be more toxic and harder to remove by adsorption than As(V).[20,21] An oxidation step is often used to convert As(III) to As(V) prior to adsorption. As(III) oxidation can be achieved through photocatalytic reaction on TiO_2[22,23] or reactions with oxidizing agents such as manganese oxide.[24] Önnby et al.[25] found that inorganic As(III) can be oxidized by H_2O_2 on Al_2O_3 via a surface-catalyzed mechanism. Fenton oxidation as a wastewater treatment technology has generated significant interest. A homogeneous Fenton reaction using ferrous ion has problems of iron ion release and iron sludge production.[26] These drawbacks can be overcome by introducing heterogeneous Fenton catalysts. Pham et al.[27] found that silica-supported iron oxide catalyzed the decomposition of H_2O_2 into oxidants capable of transforming phenol

at ~pH 3–10. Chun et al.[26] synthesized a magnetite-loaded mesocellular carbonaceous material and found that such material exhibits superior activity as both Fenton catalyst and adsorbent for phenol and arsenic removal. To the best of our knowledge, few studies have used pure iron oxide as both Fenton catalyst and adsorbent for arsenic removal.

Recently, we synthesized mesoporous Fe–Si oxide composites using Pluronic P123 as porosity-generating template, and found that the precursors of silica and iron oxide copolymerized to form a homogeneous structure with high iron content.[28] In this paper, we will show that a Fe–Si binary oxide composite could be prepared without using an organic template that may be costly, and silica units in the composite could be etched further by alkali to leave nanosized iron oxide. The main objective of this work was to study the adsorption of As(III) and As(V) on nanosized iron oxide and the catalytic oxidation-promoted adsorption of As(III) in the presence of H_2O_2.

2. Materials and methods

2.1. Chemicals

Iron nitrate nonahydrate, sodium carbonate, and tetraethyl orthosilicate (TEOS) were from Sinopharm Chemical Reagent Company Limited, Shanghai, China. Sodium arsenite ($NaAsO_2$) and sodium arsenate ($Na_2HAsO_4 \cdot 7H_2O$) were from Yikeda Chemical Reagent Corporation, Chengdu, China. All reagents were of analytical grade.

2.2. Sample preparation

In a typical synthesis, $Fe(NO_3)_3 \cdot 9H_2O$ (0.016 mol) was dissolved in 150 mL of ultrapure water. Na_2CO_3 (0.016 mol) was added under vigorous stirring to promote the partial hydrolysis of iron ions. TEOS (0.04 mmol) was added to this resultant colloidal dispersion of iron oxide precursors. The solution was stirred continuously at 40°C in a water bath for 1 day to hydrolyze TEOS, forming silica precursors and initially copolymering with the iron oxide precursors. The solution was transferred to a Teflon-lined stainless steel autoclave and heated at 100°C in an oven for 1 day to achieve further copolymerization. The solid was collected by suction filtration and washed with 1000 mL of ultrapure water, dried at 100°C and calcined at 550°C for 6 h to form a composite of Fe–Si oxide. The composite was immersed in 200 mL of 1 M NaOH at 80°C for 8 h with stirring to remove the silica species. The resultant iron oxide product was labeled nano-iron oxide.

2.3. Materials characterization

X-ray diffraction patterns were collected on a X'Pert Pro X-ray diffractometer (PANalytical, Netherlands) with Cu-Kα radiation (γ = 1.5406 Å). Transmission electron microscopy (TEM) images were taken on a JEM-2100 (JEOL, Japan) with an acceleration voltage of 200 kV. Brunauer–Emmett–Teller specific surface area (S_{BET}) was determined using a V-sorb 2800P surface area analyzer (Gold APP, China). Microscopic examinations were performed using a S-3400N scanning electron microscope (HITACHI, Japan) equipped with an energy-dispersive spectrometry microanalyzer. In order to get the point of zero charge (pH_{PZC}) of the material, 10 mL of 0.1 M NaCl solution was taken in different vials and adjusted the initial pH in the range of 4-12 with hydrochloric acid and sodium hydroxide, then 4 mg of the material was added to each vial and these vials were placed on a platform shaker for 24 h at 25°C to reach equilibrium and then the final pH of the suspension was measured, and plot the curve of the difference between initial and final pH vs initial pH, the point at which the curve crossed the pH axis determined the pH_{PZC} of the sorbent.[29,30]

2.4. Batch adsorption experiments

$NaAsO_2$ and $Na_2HAsO_4{\cdot}7H_2O$ were used as As(III) and As(V) sources, respectively. In the adsorption experiment, 10 mL of arsenic solution of a certain concentration was transferred to a 25 mL vial that contained 4 mg of adsorbent. These vials were sealed and shaken continuously on a platform shaker at 250 rpm and 25°C for 12 h to reach adsorption equilibrium. The suspension was centrifuged and the equilibrium concentrations of arsenic in the supernatant solutions were measured using an 8220 atomic fluorescence spectrophotometer (Beijing Jitian Instrument Company, China) with a total lamp current of 80 mA. High-purity argon was used as carrier and shielding gas (supplied at 300 and 800 mL/min, respectively). To detect the arsenic concentration of the arsenate solutions, a solution of ascorbic acid and thiourea was used to reduce the As(V) to As(III) prior to detection. The quantity of adsorbed arsenic at equilibrium (q_e, mg/g) was calculated as follows:

$$q_e = \frac{(C_0 - C_e)}{m} V \quad (1)$$

where C_0 (mg/L) and C_e (mg/L) represent the initial and equilibrium arsenic concentrations in solution, respectively; m (mg) is the mass of adsorbent used; and V (mL) is the solution volume.

The effect of pH on arsenic removal efficiency was evaluated by adjusting arsenic solution from pH 1 to 12 using HCl and NaOH.

The adsorption isotherms of As(III) at pH 7 and As(V) at pH 3 were obtained by varying the initial arsenic concentration from 1–100 mg/L.

Adsorption kinetic studies were conducted by varying the adsorption time from 1 to 240 min at an initial arsenic concentration of 10 mg/L. The As(III) solution was kept at pH 7, and the As(V) solution was kept at pH 3.

The influence of various competing ions, including HCO_3^-, SiO_3^-, SO_4^{2-}, HPO_4^-, Cl^-, F^-, and NO_3^-, on arsenic removal was assessed. The concentration of each competing ion was 1 mmol/L. The initial arsenic concentration was 1 mg/L (0.013 mmol/L) and As(III) and As(V) solutions were kept at pH 7 and pH 3, respectively.

Every batch experiment was repeated three times and average values were used for analysis.

2.5. Regeneration studies

To evaluate the reusability, the adsorbent were first loaded with As(III) or As(V) by stirring the suspension for 12 h with an initial arsenic concentration of 1 mg/L and with an adsorbent dosage of 0.4 g/L. After adsorption, the spent adsorbent was stirred with 1 M NaOH solution for 3 h, during which As anions could desorb from the nano-iron oxide nanoparticle surface through hydroxyl exchange and electrostatic repulsion. The adsorbent was collected by centrifugation, washed with ultrapure water, and dried in air at 100°C for the next cycle of use.

2.6. Catalytic oxidation-promoted adsorption of As(III)

Catalytic oxidation of As(III) in the presence of H_2O_2 was used to promote its adsorption. The effects of H_2O_2 concentration and pH were studied. The H_2O_2 concentration varied from 150–600 μM, and the solution acidity varied from pH 3 to 9. The dynamics of As(III) removal in the presence of 300 μM H_2O_2 was also studied. Nano-iron oxide (80 mg) was added to 200 mL of the 10 mg/L As(III) solution with stirring. The solution was sampled and the residual As(III) concentrations were analyzed after a specified time interval. Experiments were also conducted without H_2O_2 addition.

3. Results and discussion

3.1. Properties of adsorbents

Energy-dispersive spectrometry analysis revealed that the atomic Si/Fe ratio of the as-prepared composite before alkali-etching is 2.8, whereas that of nano-iron oxide is only 0.1 (Fig. S1†), which indicates that alkali-etching can dissolve silicon and leave iron oxide.

A typical TEM image of the prepared material indicates the presence of nanoparticles of less than 4 nm (Fig. 1). The X-ray diffraction pattern shows extremely weak diffraction peaks (Fig. S2†), which also

indicates that the material is composed of very small particles. On the whole, the weak diffraction peaks could be assigned to α-Fe_2O_3 (JCPDS No. 33-0664) and hydrous iron oxide FeO(OH) (JCPDS No.22–0353). Fig. 2 shows the Fe 2p XPS spectrum of the material. The Fe $2p_{2/3}$ peaks at 710.7 and 712.6 eV are attributed to Fe^{3+} bonded with O^{2-} in the crystal lattice of α-Fe_2O_3 and with −OH in FeO(OH), respectively.[31,32,33] The Fe $2p_{1/2}$ peaks at 724.2 and 725.8 eV may be assigned to α-Fe_2O_3 and FeO(OH), respectively.[31,33] Therefore, the XPS spectra also indicate that the material is a composite of α-Fe_2O_3 and FeO(OH). For the sake of simplicity, the composite of α-Fe_2O_3 and FeO(OH) is termed as nano-iron oxide in this work. A nitrogen adsorption–desorption isotherm of the nano-iron oxide is used to derive the textural properties. The isotherm features a hysteresis loop (Fig. S3†), which suggests the presence of mesopores in the samples.[34] The BJH pore size distribution profile shows that the mesopore pore size is centered at ca. 3.5 nm. The mesopores may consist of voids between the aggregated primary particles as revealed by the TEM images. It is interesting that the derived specific surface area of nano-iron oxide is 317 m^2/g, which is high compared with reported data. Analysis of the nitrogen sorption data by the t-plot method indicates that nano-iron oxide has a small internal surface area of 26 m^2/g in contrast with its external surface area of 291 m^2/g.

3.2. Effect of pH on arsenic adsorption

The pH values of arsenic solutions often influence arsenic removal. Fig. 3 shows the pH-dependence of As(III) and As(V) removal efficiency at an initial arsenic concentration of 10 mg/L and an adsorbent dosage of 0.4 g/L.

An optimal As(III) removal (~75%) was achieved at pH 6–8. A further increase in pH resulted in a sharp decrease in removal efficiency, and the As(III) removal efficiency dropped to approximately 30% at pH 12. The surface hydroxyl groups on the iron oxide can be protonated or deprotonated in solution depending on pH.[35] Fig. S4† shows that the pH_{PZC} of the nano-iron oxide is about 6.5. At pH values below the pH_{PZC}, the iron oxides would have positive surface charges because of surface hydroxyl group protonation, and above the pH_{PZC}, the reverse would occur. The pH value also determines the As(III) species structures as shown in Fig. S5a†. As(III) is present mainly as neutral H_3AsO_3 below pH 9.2, and $H_2AsO_3^-$ becomes dominant above pH 9.2. The As(III) removal efficiencies under various acidities may indicate that neutral H_3AsO_3 molecules, which exist below pH 9, could be captured more easily by iron oxide. Fe–OH and As–OH groups participate in the adsorption reactions to form either inner- or outer-sphere complexes.[36] The adsorbent manifests the highest As(III) removal efficiency at pH 6–8 possibly because, under such conditions, the iron oxide surface

has a large proportion of unaltered Fe–OH groups that favor reaction with the As–OH groups of H_3AsO_3 molecules. At other pH values that deviate from the pH_{PZC}, protonation or deprotonation of Fe–OH groups may disfavor the reaction with As–OH groups and decrease the sorption capacity. Above pH 9.2, electrostatic repulsion may occur between dominant $HAsO_3^{2-}$ species and the deprotonated negatively charged nano-iron oxide surface, which hinders arsenic adsorption.

The As(V) removal efficiency was almost 100% at pH 2−4, it decreased gradually with increase in pH from 4 to 10, and a large decrease in removal efficiency occurred with further increase in pH to 11. Fig. S5b† shows the species variation of As(V) with pH. Neutral H_3AsO_4 molecules are dominant species in solution only below pH 2, and they almost disappear above pH 4. From pH 2−12, As(V) is present mainly as negative $H_2AsO_4^-$, $HAsO_4^{2-}$, and AsO_4^{3-}, and higher pH values indicate that more hydroxyl groups on H_3AsO_4 molecules dissociate to induce negative charges. In literature, it is suggested that at pH < 4.3, positively charged adsorbent surfaces favor As(V) adsorption by electrostatic attraction between $H_2AsO_4^-$ anions and surface $-OH_2^+$.[37] It is not clear in this work why, from pH 8–10, the adsorbent surface is still capable of removing more than 60% As(V) despite the repulsive forces between negatively charged deprotonated surface and arsenic anions. We suggest that the As–OH groups also play an important role in As(V) adsorption. At pH 2−4, dominant $H_2AsO_4^-$ and H_3AsO_4 species that contain more As–OH groups could be captured more easily by iron oxide. However, the dissociation of As–OH at higher pH hinders their reaction with Fe–OH: for pH > 11, dominant AsO_4^{3-} species contain no As–OH groups, which results in a very poor arsenate uptake.

3.3. Adsorption isotherms

Fig. 4a shows the adsorption isotherm of As(III) at pH 7 and that of As(V) at pH 3. Langmuir (Fig. 4b) and Freundlich (Fig. 4c) models were used to fit the experimental data.

The Langmuir model is derived from the hypothesis that the adsorbent surface is homogeneous and adsorbs only monolayer adsorbates without involving intermolecular forces.[38,39] The mathematical linear expressions of the Langmuir isotherm can be written as:

$$\frac{1}{Q_e} = \frac{1}{Q_m} + \frac{1}{bQ_mC_e} \quad (2)$$

where C_e (mg/L) is the equilibrium arsenic concentration, Q_e (mg/g) is the equilibrium adsorption capacity, Q_m (mg/g) is the maximum sorption capacity, and b (L/mol) is the affinity of binding sites.

The Freundlich isotherm is derived by assuming a heterogeneous surface with a nonuniform distribution of the heat of sorption over the surface. Its linearized form can be expressed by the following formula:

$$lnQ_e = lnK_f + \frac{1}{n} lnC_e \quad (3)$$

where C_e (mg/L) is the equilibrium concentration of arsenic, Q_e (mg/g) is the equilibrium adsorption capacity, and K_f (mg/g) and n are the Freundlich experimental constants related to the adsorption capacity and the adsorption intensity, respectively.

The isotherm parameters and correlation coefficients obtained by nonlinear regression analyses with both models are listed in Table 1. The correlation coefficients indicate that the As(III) and As(V) adsorption data could be better fitted into the Langmuir model than the Freundlich one. The maximum adsorption capacity derived from the Langmuir isotherms for As(III) and As(V) is 42 and 83 mg/g, respectively.

The adsorption capacities of the samples for As(III) and As(V) in this work were compared with other nanostructured iron oxide materials reported in literature as shown in Table 2. The results indicate that nano-iron oxide possesses a relatively high sorption capacity for As(III) and As(V).

3.4. Kinetics of arsenic adsorption

Fig. 5a shows the As(III) uptake at pH 7 and As(V) uptake at pH 3 with time on stream. The As(III) adsorption reached equilibrium in 120 min, whereas that of As(V) was reached in 50 min. This indicates that nano-iron oxide is more favorable for As(V) removal than As(III), which agrees with the sorption isotherm results.

The kinetics of As(III) and As(V) adsorption were evaluated using pseudo-first- and -second-order models. The pseudo-first-order model can be written as:[44]

$$ln(Q_e - Q_t) = lnQ_e - k_1 t \quad (4)$$

The pseudo-second-order model that represents sorption processes controlled by chemical reaction can be expressed as follows:[45,46]

$$\frac{t}{Q_t} = \frac{1}{k_2 Q_e^2} + \frac{1}{Q_e} t \quad (5)$$

The initial sorption rate h can be defined as:

$$h = k_2 Q_e^2 \quad (6)$$

In the two models, k_1 is the rate constant of pseudo-first-order adsorption and k_2 is that of pseudo-second-order adsorption, Q_e is the equilibrium adsorption capacity, and Q_t is the amount of adsorbate adsorbed at time t.

The fitted curves based on the two kinetic models are displayed in Fig. 5b and Fig. 5c, and kinetic parameters calculated from experimental data are listed in Table 3. The correlation coefficients suggest that the pseudo-second-order kinetic model fitted better for As(III) and As(V) adsorption, which indicates that chemisorption took place during arsenic uptake onto nano-iron oxide.[30,46-48] The initial sorption rate for As(V) is approximately seven times faster than that for As(III) (Table 3), which also indicates that nano-iron oxide has a better affinity for the former.

An intraparticle diffusion model[30,49] was used to reveal the rate-determining step for arsenic adsorption. The validity of this model is confirmed by linear plots of the Weber and Morris equation:

$$Q_t = k_p t^{0.5} + c \quad (7)$$

where Q_t is the amount of adsorbate adsorbed at time t, k_p is the intraparticle diffusion rate constant, and the intercept c is associated with the boundary layer effect. If the plot of Q_t versus $t^{0.5}$ is linear and passes through the origin, then intraparticle diffusion is the rate-limiting step, otherwise it is not the only rate-limiting step.[30,49] A larger intercept value c represents a greater boundary layer effect and a greater contribution of boundary layer diffusion in the rate-controlling step.[30]

Linear plots of the intraparticle diffusion model for arsenic are shown in Fig. 6a and the derived parameters are shown in Table 4. Plots for As(III) and As(V) do not pass through the origin, which indicates that intraparticle diffusions were not the only rate-limiting step.[30] In many reported works, linear plots of the intraparticle diffusion model could be divided into three steps, namely, the first sharper portion that reflected the external surface adsorption stage, where boundary layer diffusion of solute molecules was rate-controlled, the second gradual portion that reflected the internal surface adsorption stage, where intraparticle diffusion was rate-controlled, and the third horizontal portion that reflected the adsorption equilibrium stage. In this work, only two steps are observed for As(III) and As(V) as shown in Fig. 6a. The first sharper sections represent arsenic diffusion to the external adsorbent surface and occupation of the readily available adsorption sites.[20] The second parts are horizontal, which indicates that equilibrium has been reached. The intercept c for As(V) is greater than that for As(III), which suggests that a greater boundary layer effect occurred in As(V) adsorption.[30] Because As(V) could be captured more easily by iron oxide, its

concentration in the boundary layer would be lower. Therefore, diffusion of As(V) from the bulk solution to the particle surface would influence the adsorption rate more significantly.

General adsorbents often possess framework-confined pores and intraparticle surfaces. However, tiny iron oxide nanoparticles possess dominant external surfaces instead of internal surfaces. Furthermore, the nanoparticles can be well-dispersed in water and their surfaces are easily approachable. Because most adsorption sites are located on the external surfaces of nano-iron oxide, intraparticle adsorption may be negligible.

An external diffusion model[50] was also used to fit the experimental data before reaching equilibrium. This model can be expressed as:

$$ln\frac{C_t}{C_0} = -k_f \frac{A}{V}t \quad (8)$$

where C_0, C_t, A/V, t, and k_f are the initial adsorbate concentration, concentration at time t, ratio of the external sorption area to the total solution volume, sorption time, and external diffusion coefficient, respectively. If the adsorption is controlled by external resistance, a plot of $\ln C_t/C_0$ versus t must be linear.

Linear plots of the external diffusion model for arsenic are shown in Fig. 6b and the derived parameters are shown in Table 4. The plots for As(III) and As(V) pass through the origin, which indicates that the external diffusions were the rate-limiting step in arsenic adsorption.

3.5. Effect of coexisting ions and ionic strength on As(III) and As(V) sorption

The competing effect induced by co-existing anions on arsenic removal was studied, and the results are shown in Fig. 7a. Even though the concentration of competing ions (1 mmol/L) was much higher than that of arsenic (0.013 mmol/L), the presence of HCO_3^-, SO_4^{2-}, Cl^-, F^-, and NO_3^- did not have any effect on arsenic adsorption. In contrast, the presence of HPO_4^{2-} and SiO_3^{2-} showed some deterioration effect, especially for HPO_4^{2-}. Silicate and hydrophosphate tend to retain multi-hydroxyl groups in aqueous system, and these hydroxyl groups may compete with arsenic and react with surface groups on the adsorbent.[51]

The effect of ionic strength on As(III) and As(V) removal is shown in Fig. 7b. The arsenic removal remained almost constant when the ionic strength increased from 0.001 M $NaNO_3$ to 0.1 M $NaNO_3$, which indicates that arsenic adsorption on nano-iron oxide is unaffected by change in ionic strength. Goldberg et al.[36] proposed that inner-sphere surface complexation could be a dominant process if the adsorption exhibits either no ionic strength dependence or an increasing adsorption with increasing solution ionic strength. Outer-sphere

complexation could be dominant if the adsorption decreases with increasing ionic strength. According to this theory, the As(III) and As(V) adsorption onto nano-iron oxide is dominated by inner-sphere complexation.

3.6. Mechanism of As(III) and As(V) removal

Studies of adsorption kinetics and the effect of ionic strength suggest that arsenic removal on nano-iron oxide may be by chemisorption via inner-sphere surface complexation. Goldberg et al.[36] summarized the surface reactions for arsenic adsorption on oxides by inner-sphere surface complexation as follows:

$$FeOH_{(s)} + H_3AsO_{4\,(aq)} \rightleftharpoons FeH_2AsO_{4\,(s)} + H_2O \quad (9)$$

$$FeOH_{(s)} + H_3AsO_{4\,(aq)} \rightleftharpoons FeHAsO^{-}_{4\,(s)} + H^{+}_{(aq)} + H_2O \quad (10)$$

$$FeOH_{(s)} + H_3AsO_{4\,(aq)} \rightleftharpoons FeAsO^{2-}_{4\,(s)} + 2H^{+}_{(aq)} + H_2O \quad (11)$$

$$FeOH_{(s)} + H_3AsO_{3\,(aq)} \rightleftharpoons FeH_2AsO_{3\,(s)} + H_2O \quad (12)$$

$$FeOH_{(s)} + H_3AsO_{3\,(aq)} \rightleftharpoons FeHAsO^{-}_{3\,(s)} + H^{+}_{(aq)} + H_2O \quad (13)$$

In all cases, Fe–OH and As–OH groups participate in the adsorption reactions. Therefore it is not surprising that an improved arsenic removal efficiency was achieved when arsenic species and iron oxide contain more hydroxyl groups at suitable pH conditions as discussed previously. Previous researches have suggested that arsenic removal may depend on the surface density of hydroxyl groups on iron oxides, which can form complexes with arsenite and arsenate.[52-54]

Adsorbent X-ray photoelectron spectroscopy (XPS) spectra were recorded to reveal the adsorption mechanism. Fig. 8 shows a wide-scan XPS spectrum of the O 1s binding energies of the adsorbent before and after adsorbing arsenic. The O 1s spectrum can be divided into three component peaks with binding energies of ~530, ~531, and ~532 eV, which can be assigned to O in the form of metal oxide (M–O), hydroxyl group bonded to metal (M–OH) and adsorbed water (H_2O), respectively.[55-57] After As(III) and As(V) adsorption, the relative ratios of M–OH decreased, which indicates that some surface hydroxyl groups were consumed in surface reactions. The relative ratios of M–O increased after adsorption, which could be attributed to the introduction of As–O after surface reactions. Therefore, the XPS spectra verified that the hydroxyl groups on nano-iron oxide reacted with those on arsenic species during adsorption, to form inner-sphere complexes.

3.7. Regeneration studies

For practical adsorbent use, a high efficiency of adsorbent regeneration and reusability is very important. In this work, the used adsorbent was regenerated in aqueous alkali solution. Fig. 9 shows the efficiency of

As(III) or As(V) removal by nano-iron oxide nanoparticles during five adsorption–regeneration cycles. The removal efficiency after five cycles remained almost unchanged, which indicated that the adsorbent could be easily regenerated and is promising for practical applications.

3.8. Catalytic oxidation-promoted As(III) removal

H_2O_2 was used to induce As(III) oxidation to promote its adsorptive removal. By varying H_2O_2 concentrations from 0 to 600 μM at pH 7, it was found that optimal As(III) removal was achieved at a H_2O_2 concentration of 300 μM (Fig. S6†). Above 300 μM, the As(III) removal efficiency no longer increased and even showed a slight decrease because the higher-concentration H_2O_2 can scavenge •OH radicals.[58] Fig.10 shows the XPS spectra of the As 3d binding energies of the spent adsorbents. The As 3d binding energies for As(III) and As(V) were reported to be 44.3–44.5 and 45.2–46.1 eV, respectively.[59,60] In the absence of H_2O_2, the As 3d binding energy of the spent adsorbent was 44.5 eV, indicating it is As(III). In the presence of 300 μM H_2O_2, it was shifted to 45.7 eV, indicating that As(III) was converted into As(V).

Fig. 11 shows the As(III) removal on nano-iron oxide with time on stream in the presence and absence of 300 μM H_2O_2 at various pH values. Within pH 3–9, the addition of H_2O_2 promoted As(III) removal, which could be attributed to the simultaneous oxidation and adsorption of As(III). It should be mentioned that As(III) oxidation in aqueous H_2O_2 solution without metal oxide is very slow and requires up to 30 d.[61] In this work, nano-iron oxide might catalyze fast As(III) oxidation, and it played a dual role of catalyst and adsorbent. At pH 11, H_2O_2 actually declined the arsenic removal. As discussed previously, under highly alkaline conditions, the severe dissociation of hydroxyl groups on As(V) species could hinder arsenic adsorption onto iron oxide surfaces, and the As(V) uptake was even lower than As(III) at pH 11 (Fig. 3). Therefore, due to conversion of As(III) to As(V) in the presence of H_2O_2, the arsenic removal declined at pH 11.

It is well known that Fe^{2+} is capable of catalyzing H_2O_2 decomposition to generate oxidative hydroxyl radicals. We added Fe^{2+} to the nano-iron oxide and H_2O_2 system, and found that a higher As(III) removal rate was achieved in the presence of 600 μM Fe^{2+} (Fig. 12). This indicates that H_2O_2 coupled with Fe^{2+} could promote As(III) oxidation. Furthermore, spontaneous sedimentation of nano-iron oxide in water was slow, most likely because of their small particle sizes and good dispersion in water; however, if Fe^{2+} were present, sedimentation was more rapid and most likely because the ionic iron species could act as a flocculation agent. This could be helpful in practical applications because adsorbent can be separated easily.

4. Conclusions

Nanosized iron oxide was prepared by an etching method and used as an adsorbent for effective As(III) and As(V) removal from water. The nanosized iron oxide had a high specific surface area of 317 m^2/g and primary particle size of approximately 4 nm. Arsenic adsorptions were pH dependent, and pH 6–8 and 2–4 are most favorable for As(III) and As(V) removal, respectively. As(III) and As(V) adsorption could be fitted well into the Langmuir model, and the maximum adsorption capacity for As(III) and As(V) was 42 mg/g and 83 mg/g, respectively. The adsorption kinetics obeyed a pseudo-second-order model and the rate-limiting step was external diffusion. Phosphate and silicate anions decreased the arsenic removal to some extent, whereas other co-existing anions and ionic strengths had no effect on arsenic removal. The mechanism of arsenic removal on nano-iron oxide may be chemisorption via inner-sphere surface complexation, and hydroxyl groups on the iron oxide and arsenic species were involved in adsorption. As(III) removal can be promoted by catalytic oxidation in the presence of H_2O_2. The high arsenic uptake capability of nanosized iron oxide makes it a potentially attractive adsorbent for arsenic removal from aqueous solution.

Acknowledgments

This work was supported by the National Natural Science Foundation of China (21477090 and 21477092) and the Natural Science Foundation of Hubei Province (2014CFB182).

References

1 D. Setyono and S. Valiyaveettil, *RSC Adv.*, 2014, **4**, 53365–53373.

2 Y. F. Lin and J. L. Chen, *RSC Adv.*, 2013, **3**, 15344-15349.

3 S. Zavareh, M. Zarei, F. Darvishi and H. Azizi, *Chem. Eng. J.*, 2015, **273**, 610–621.

4 T. Mahmood, S. U. Din, A. Naeem, S. Mustafa, M. Waseem and M. Hamayun, *Chem. Eng. J.*, 2012, **192**, 90–98.

5 K. Babaeivelni, A. P. Khodadoust and D. Bogdan, *J. Environ. Sci. Heal. A*, 2014, **49**, 1462–1473.

6 J. Zhu, Z. Lou, Y. Liu, R. Fu, S. A. Baig and X. Xu, *RSC Adv.*, 2015, **5**, 67951-67961.

7 T. S. Y. Choong, T. G. Chuah, Y. Robiah, F. L. Gregory Koay and I. Azni, *Desalination*, 2007, **217**, 139–166.

8 Z. Zhao, Y. Jia, L. Xu and S. Zhao, *Water Res.*, 2011, **45**, 6496–6504.

9 C. M. Iesan, C. Capat, F. Ruta and I. Udrea, *Water Res.*, 2008, **42**, 4327–4333.

10 P. Z. Ray and H. J. Shipley, *RSC Adv.*, 2015, **5**, 29885-29907.

11 W. Tang, Q. Li, S. Gao and J. K. Shang, *J. Hazard. Mater.*, 2011, **192**, 131–138.

12 J. Saiz, E. Bringas and I. Ortiz, *J. Chem. Tech. Biotechnol.*, 2014, **89**, 909–918.

13 W. Cheng, J. Xu, W. Ding, Y. Wang, W. Zheng, F. Wu and J. Li, *Mater. Chem. Phys.*, 2015, **153**, 187–194.

14 F. Mou, J. Guan, Z. Xiao, Z. Sun, W. Shi and X. Fan, *J. Mater. Chem.*, 2011, **21**, 5414–5421.

15 S. Mandal and A. H. E. Müller, *Mater. Chem. Phys.*, 2008, **111**, 438–443.

16 L. M. Bronstein, J. E. Atkinson, A. G. Malyutin, F. Kidwai, B. D. Stein, D. G. Morgan, J. M. Perry and J. A. Karty, *Langmuir*, 2011, **27**, 3044–3050.

17 Y. Tan, Z. Zhuang, Q. Peng and Y. Li, *Chem. Mater.*, 2008, **20**, 5029–5034.

18 F. Mou, J. Guan, H. Ma, L. Xu and W. Shi, *ACS Appl. Mater. Inter.*, 2012, **4**, 3987–3993.

19 J. Liu, S. Z. Qiao, Q. H. Hu and A. G. Q. M. Lu, *Small*, 2011, **4**, 425–443.

20 I. Jacukowicz-Sobala, D. Ociński and E. Kociołek-Balawejder, *Ind. Eng. Chem. Res.*, 2013,**52**, 6453–6461.

21 X. Yu, R. Xu, C. Gao, T. Luo, Y. Jia, J. Liu and X. Huang, *ACS Appl. Mater. Inter.*, 2012, **4**, 1954–1962.

22 S. M. Miller and J. B. Zimmerman, *Water Res.*, 2010, **44**, 5722–5729.

23 G. Zhang, M. Sun, Y. Liu, X. Lang, L. Liu, H. Liu, J. Qu and J. Li, *ACS Appl. Mater. Inter.*, 2015, **7**, 511–518.

24 G. Zhang, J. Qu, H. Liu, R. Liu and G. Li, *Environ. Sci. Technol.*, **41**,2007, 4613–4619.

25 L. Önnby, P. S. Kumar, K. G. V. Sigfridsson, O. F. Wendt, S. Carlson and H. Kirsebom, *Chemosphere*, 2014, **113**, 151–157.

26 J. Chun, H. Lee, S. Lee, S. Hong, J. Lee, C. Lee and J. Lee, *Chemosphere*, 2012, **89**, 1230–1237.

27 A. L. Pham, C. Lee, F. M. Doyle and D. L. Sedlak, *Environ. Sci. Technol.*, 2009, **43**, 8930–8935.

28 W. Zhang, X. Lu, W. Zhou, F. Wu and J. Li, *Chinese Sci. Bull.*, 2014, **59**, 4008–4013.

29 M. Mullet, P. Fievet, A. Szymczyk, A. Foissy , J.C. Reggiani and J. Pagetti, *Desalination*,1999, **121**, 41-48.

30 M. Hamayun, T. Mahmood, A. Naeem, M. Muska, S. U. Din and M. Waseem, *Chemosphere*, 2014, **99**, 207–215.

31 J. D. Walker and R. Tannenbaum, *Chem. Mater*., 2006, **18***,* 4793-4801.

32 L. L. Tian, M. J. Zhang, C. Wu, Y. Wei, J. X. Zheng, L. P. Lin, J. Lu, K. Amine, Q. C. Zhuang and F. Pan, *ACS Appl. Mater. Interf.*, 2015, **7**, 26284-26290.

33 B. J. Tan, K. J. Klabunde, and P. M. **A.** Sherwood, *Chem. Mater.,* 1990, **2***,* 186-191.

34 K. S. W. Sing, D. H. Everett, R. A. W. Haul, L. Moscou, R. A. Pierotti, J. Rouquerol and T. Siemieniewska, *Pure Appl. Chem.*, 1984, **57**, 603–619.

35 Z. Li, S. Deng, G. Yu, J. Huang and V. C. Lim, *Chem. Eng. J.*, 2010, **161**, 106–113.

36 S. Goldberg and C. T. Johnston, *J. Colloid Interface Sci.*, 2001, **234**, 204–216.

37 S. Kumar, R. R. Nair, P. B. Pillai, S. N. Gupta, M. A. R. Iyengar and A. K. Sood, *ACS Appl. Mater. Inter.*, 2014, **6**, 17426–17436.

38 Y. Kim, C. Kim, I. Choi, S. Rengaraj and J. Yi, *Environ. Sci. Technol.*, 2004, **38**, 924–931.

39 X. Sun, C. Hu, X. Hu, J. Qu and M. Yang, *J. Chem. Tech. Biotechnol.*, 2013, **88**, 629–635.

40 Y. Tian, M. Wu, X. Lin, P. Huang and Y. Huang, *J. Hazard. Mater.*, 2011, **193**, 10–16.

41 K. P. Raven, A. Jain and R. H. Loeppert, *Environ. Sci. Technol.,* 1998, **32**, 344-349.

42 B. J. Lafferty and R. H. Loeppert, *Environ. Sci. Technol.*, 2005, **39**, 2120-2127.

43 H. Lu, Z. Zhu, H. Zhang, J. Zhu and Y. Qiu, *Chem. Eng. J.*, 2015, **276**, 365–375.

44 S. Azizian, *J. Colloid Interface Sci.*, 2004, **276**, 47–52.

45 Y. Ho, *J. Hazard. Mater.*, 2006, **136**, 681–689.

46 Y. S. Ho and G. McKay, *Process Biochem.*, 1999, **34**, 451–465.

47 E. Kim, C. Lee, Y. Chang and Y. Chang, *ACS Appl. Mater. Inter.*, 2013, **5**, 9628–9634.

48 A. Yürüm, Z. Ö. Kocabaş-Ataklı, M. Sezen, R. Semiat and Y. Yürüm, *Chem. Eng. J.*, 2014, **242**, 321–332.

49 C. K. Ahn, D. Park, S. H. Woo and J. M. Park, *J. Hazard. Mater.*, 2009, **164**, 1130–1136.

50 C. K. Lee, K. S. Low and S. L. Chew, *Adv. Environ. Res.*, 1999, **3**, 343–351.

51 W. Cheng, J. Xu, Y. Wang, F. Wu, X. Xu and J. Li, *J. Colloid Interface Sci.*, 2015, **445**, 93–101.

52 S. Fendorf, M. J, P. Eick and D. L. Sparks, *Environ. Sci. Technol.*, 1997, **31**, 315–320.

53 P. R. Grossl, M. EIck, D. L. Sparks, S. Goldberg and C. C. Ainsworth, *Environ. Sci. Technol.*, 1997, **31**, 321–326.

54 X. Guo, Y. Du, F. Chen, H. Park and Y. Xie, *J. Colloid Interface Sci.*, 2007, **314**, 427–433.

55 E. A. Deliyanni, L. Nalbandian and K. A. Matis, *J. Colloid Interface Sci.*, 2006, **302**, 458–466.

56 Y. Zhang, M. Yang, X. Dou, H. He and D. Wang, *Environ. Sci. Technol.*, 2005, **39**, 7246–7253.

57 S. Deng, H. Liu, W. Zhou, J. Huang and G. Yu, *J. Hazard. Mater.*, 2011, **186**, 1360–1366.

58 M. J. Thomas, M. W. Sutherland, R. L. Arudi and B. H. Bielski, *Arch. Biochem. Biophys.*, 1984, **233**, 772–775.

59 Z. Ren, G. Zhang and J. P. Chen, *J. Colloid Interface Sci.*, 2011, **358**, 230–237.

60 M. Fantauzzi, D. Atzei, B. Elsener, P. Lattanzi and A. Rossi, *Surf. Interface Anal.*, 2006, **38**, 922–930.

61 M. Pettine, L. Campanellal and F. J. Millero, *Geochim. Cosmochim. Ac.*, 1999, **63**, 2727–2735.

List of tables

1

2 **Table 1** Isotherm parameters for As(III) and As(V) adsorption

	Langmuir isotherm			Freundlich isotherm		
	Q_m (mg/g)	b (L/mg)	R^2	K_f (mg/g)	n	R^2
As(III)	42	0.4	0.9789	11.3	2.1	0.9214
As(V)	83	0.8	0.9989	28.6	3.1	0.8288

3

4

Table 2 Arsenic adsorption capacity compared with other iron oxide materials

Adsorbents	Specific surface area (m^2/g)	Adsorption capacity (mg/g)		Initial As concentration (mg/L)		Ref.
		As(III)	As(V)	As(III)	As(V)	
Nano-iron oxide	317	42	83	1–100	1–100	This study
Fe_3O_4 loaded PCL	–	32	28	10–80	10–80	1
Ultrafine α-Fe_2O_3	162	95	47	0–200	0–200	11
γ-Fe_2O_3–TiO_2	154	33	–	0.1–50	–	22
Fe_3O_4-silica	294	14.7	121	5–750	5–750	12
Magnetic wheat Straw	4.7	3.9	8.1	1–28	1–28	40
Resin/FeMn	48	13.5	14.5	5–150	5–200	20
Ascorbic acid-coated Fe_3O_4	179	46.1	16.6	0–70	0–50	21
Ferrihydrite	202	526.4	219.3	20-2000	20-2000	41
Ferrihydrite	–	175.5	135.8	0-150	0-150	42
Zn–Fe-LDH	11.9	–	151.4	–	2-100	43

1

2 **Table 3** Kinetic parameters for arsenic adsorption

	Pseudo-first order			Pseudo-second order			
	k_1 (min^{-1})	Q_e (mg/g)	R^2	k_2 (g mg^{-1} min^{-1})	Q_e (mg/g)	h (mg g^{-1} min^{-1})	R^2
As(III)	0.018	11.0	0.9779	0.0036	19.5	1.4	0.9976
As(V)	0.073	15.2	0.9280	0.017	23.7	9.6	0.9993

3

4

Table 4 Internal and external diffusion model parameters for arsenic adsorption

	Internal diffusion model			External diffusion model	
	k_p (mg g^{-1} min$^{-0.5}$)	C(mg g^{-1} min$^{-0.5}$)	R^2	k_f (cm/min)	R^2
As(III)	1.4	4.1	0.9889	5.8×10^{-5}	0.9922
As(V)	2.1	10	0.9733	1.6×10^{-5}	0.9907

List of Figures

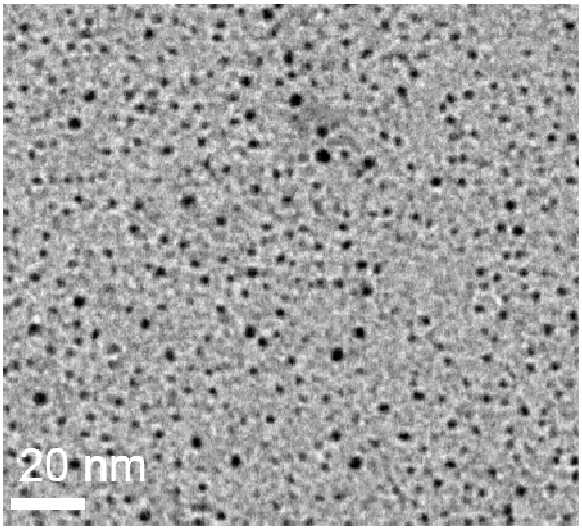

Fig. 1 TEM image of nano-iron oxide.

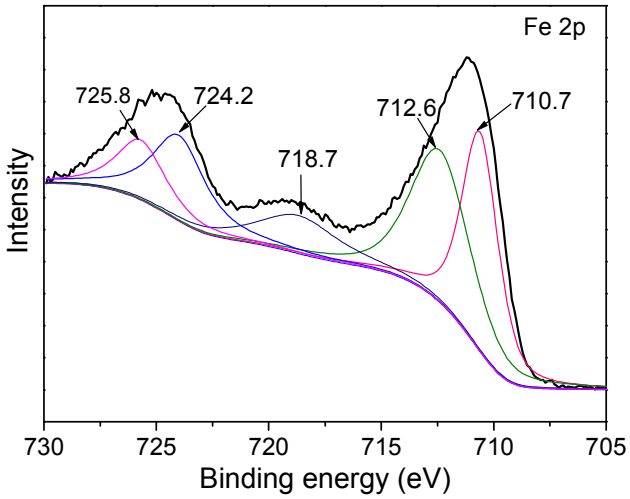

Fig. 2 Wide-scan X-ray photoelectron spectroscopy spectrum of the Fe 2p binding energies of nano-iron oxide.

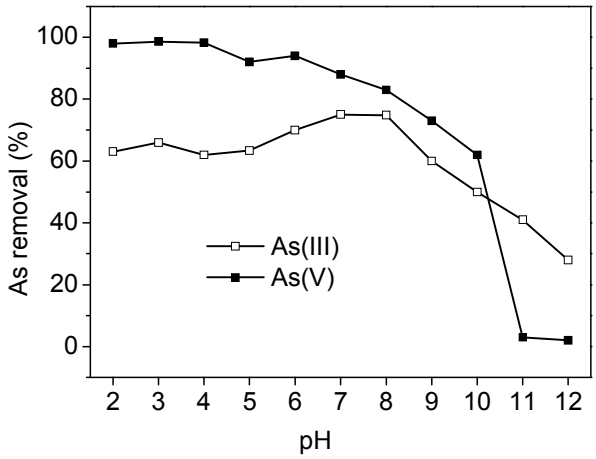

Fig. 3 Influence of pH on As(III) and As(V) adsorption.

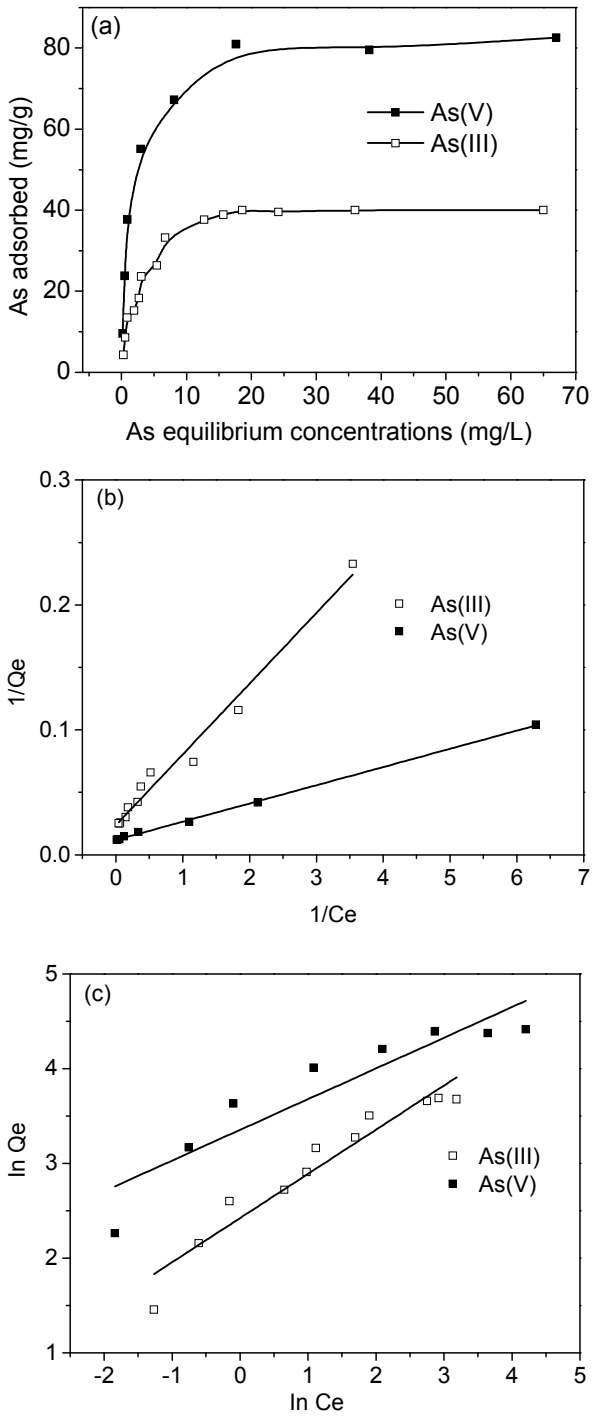

Fig. 4 (a) Arsenic adsorption isotherms at 25°C, (b) Langmuir isotherm plots, and (c) Freundlich isotherm plots.

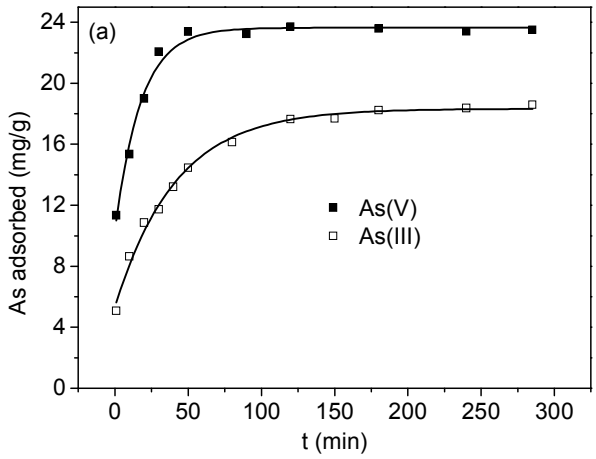

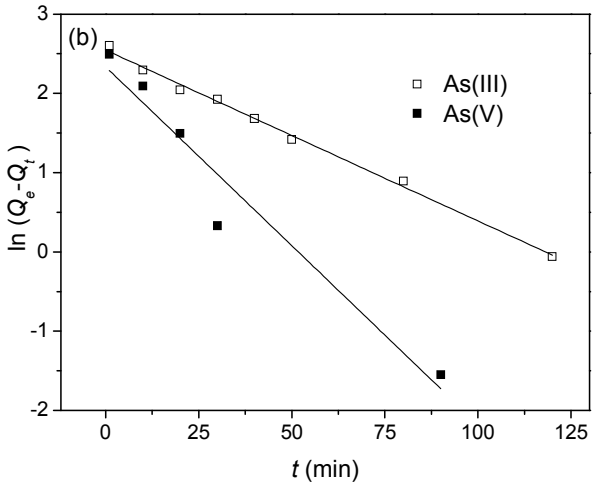

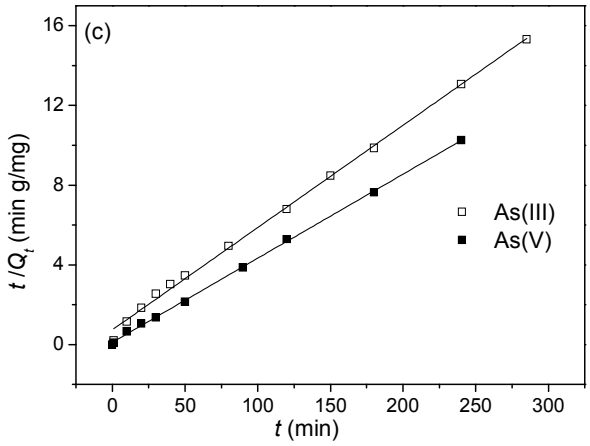

Fig. 5 Kinetics of arsenic adsorption: (a) arsenic uptake with time on stream, (b) pseudo-first-order kinetic model, and (c) pseudo-second-order kinetic model.

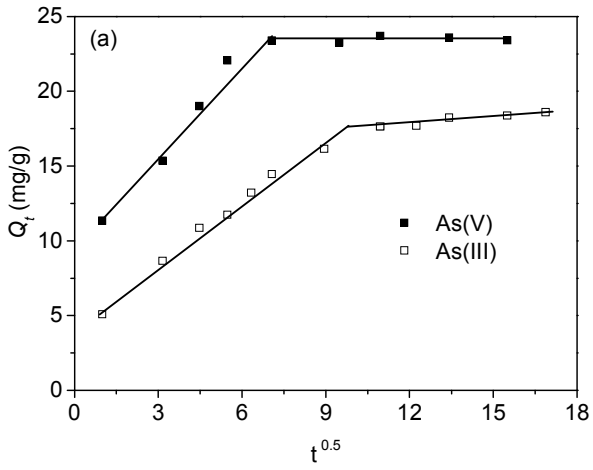

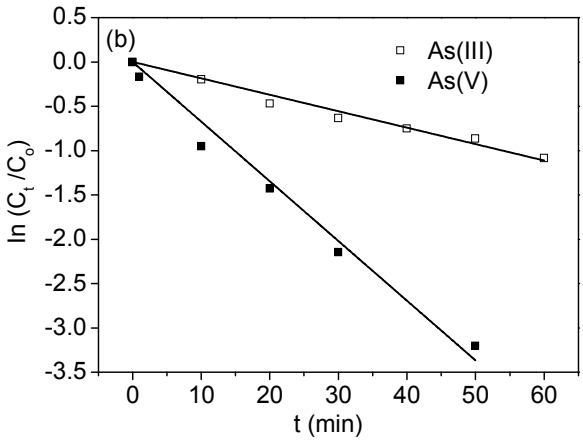

Fig. 6 (a) Intraparticle model and (b) external diffusion models.

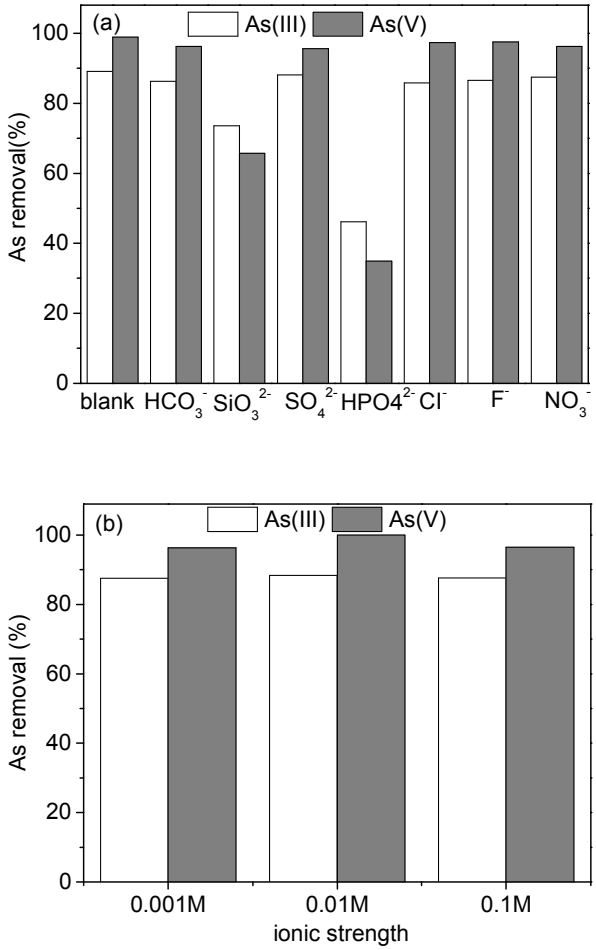

Fig. 7 Effect of (a) coexisting ions and (b) ionic strength on As removal.

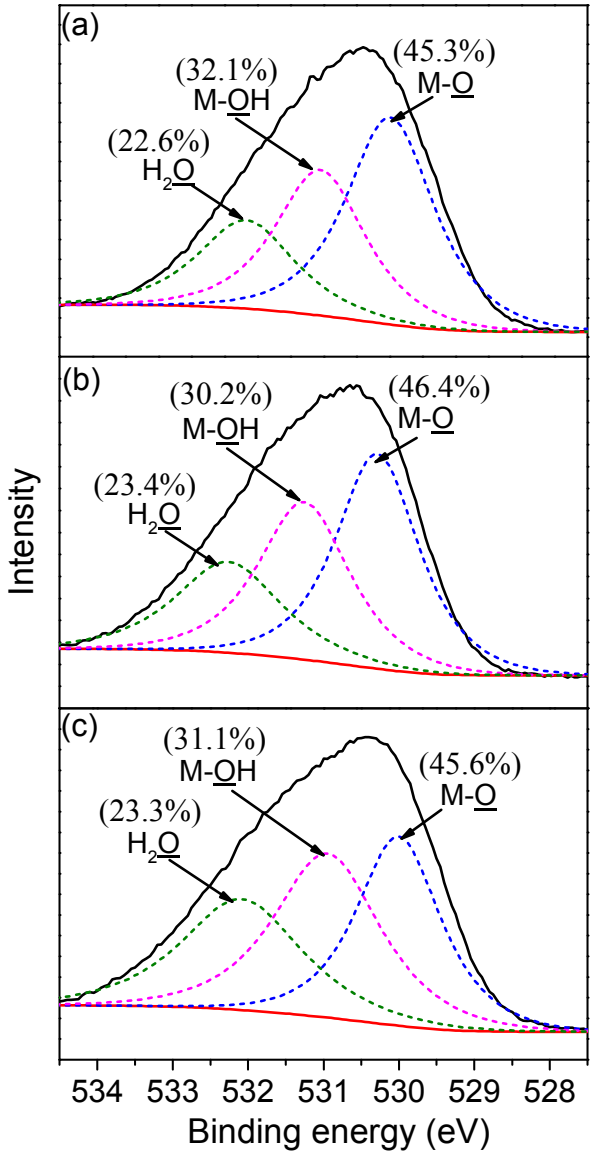

Fig. 8 Wide-scan X-ray photoelectron spectroscopy spectra of the O 1s binding energies of (a) fresh, (b) As(III)-adsorbed, and (c) As(V)-adsorbed adsorbent.

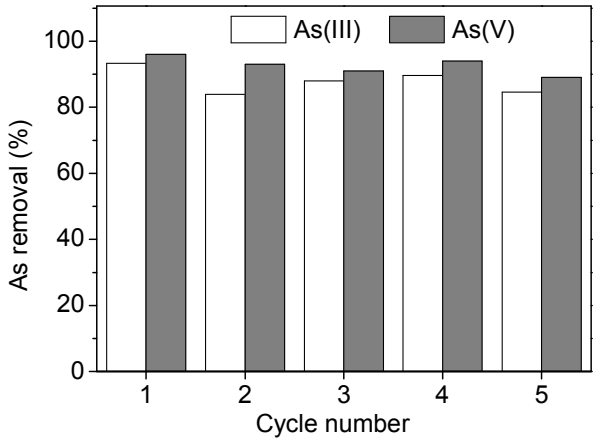

Fig. 9 As(III) and As(V) removal efficiency on regenerated nano-iron oxide.

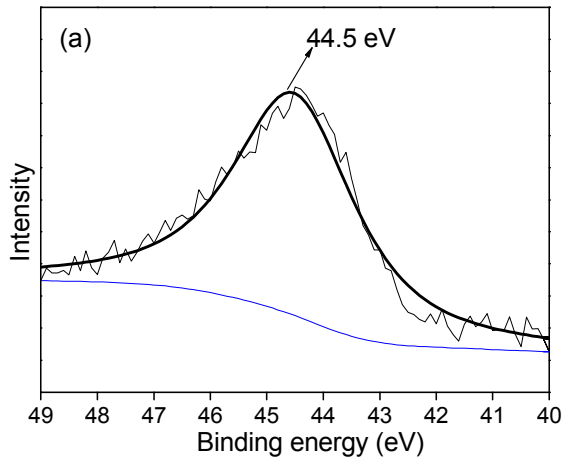

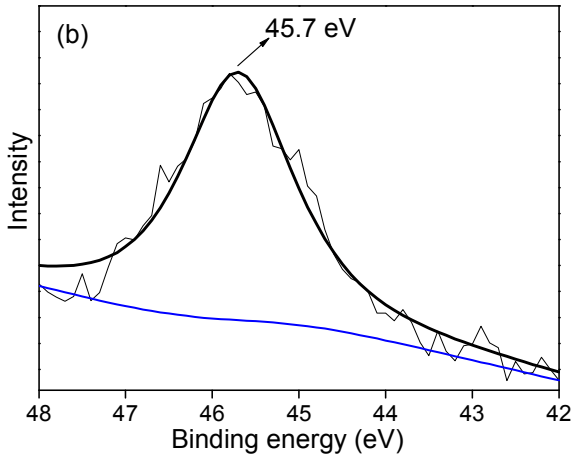

Fig. 10 Wide-scan X-ray photoelectron spectroscopy spectra of the As 3d binding energies of the adsorbent after adsorbing As(III) (a) in the presence and (b) absence of H_2O_2.

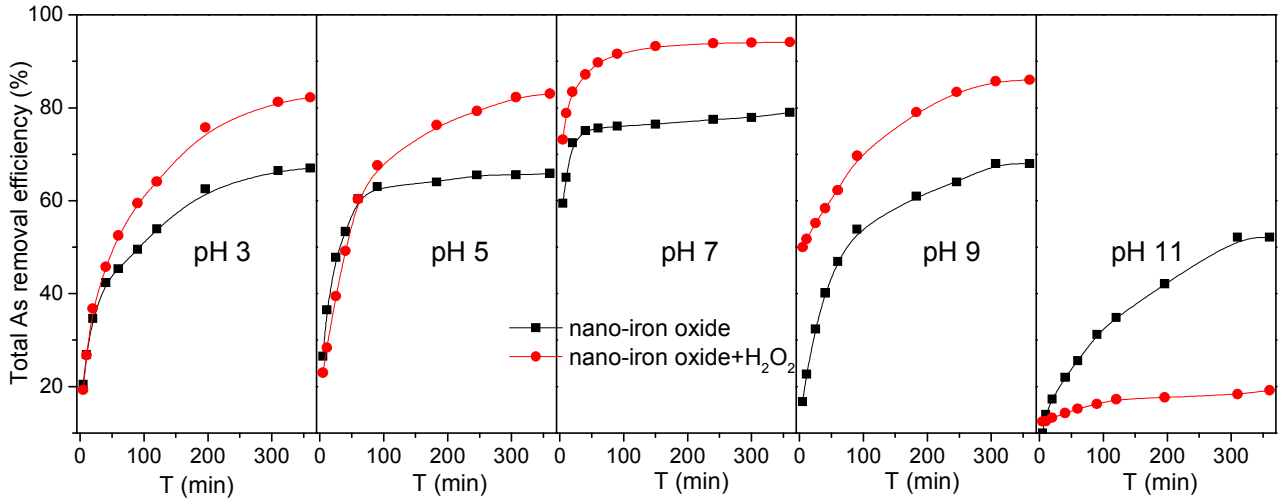

Fig. 11 Total arsenic removal with time on stream in the presence and absence of H_2O_2.

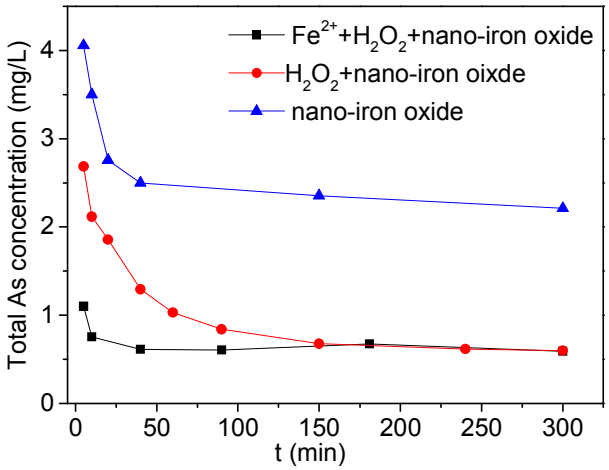

Fig. 12 Change in total arsenic concentration with time on stream (pH 7, initial concentrations: As(III) = 10 mg/L, H_2O_2 = 300 μM, Fe^{2+} = 600 mM).